Ray tracing based reconstruction of PIV measurements in the outlet zone of gaseous flow in packed beds

C. Velten[1,*], M. Ebert[2], C. Lessig[2], K. Zähriger[1]

1: Lab. of Fluid Dynamics and Technical Flows, Otto-von-Guericke-University Magdeburg, Germany
2: Dept. of Computer Science, Otto-von-Guericke-University Magdeburg, Germany
* Correspondent author: christin.velten@ovgu.de

Keywords: Particle Image Velocimetry (PIV), ray tracing, image correction, packed bed, spherical packing, air flow

ABSTRACT

The flow characteristics of packed beds are essential for the optimization of heat and mass transfer in countless industrial processes. In this study a method is introduced to allow optical measurement techniques in a transparent bulk reactor, so that optical distortions are corrected by a ray tracing based reconstruction. The velocity of the gas flow is measured by a classical particle image velocimetry measurement approach, where the distorted raw particle images, obtained through the transparent spheres, are corrected by a ray tracing step before a common cross-correlation evaluation of the velocity fields. Special calibration procedures, linking the exact geometrical set-up of the measurement equipment with respect to the packed bed reactor to the numerical model used for distortion correction, are necessary for this approach, which is validated in this study at the outlet flow field of the bed. The main principles like the experimental setup, calibration and correction method are presented and discussed, as well as the precision of the initial flow field obtained in the experimental symmetric reactor. Results of flow fields at the surface of a 17 layer transparent packed bed for particle Reynolds numbers in the range of 200 to 500 show the impact and advantages of the additional ray tracing step. A validation of the ray tracing based correction method is shown by comparing the flow of the freeboard, obtained from undistorted particle images, to the flow field behind spheres, which initially cause strong optical distortions in the raw particle images. The continuously evolving velocity profiles, through regions of originally strong optical distortion, show the applicability of the method even for the reconstruction of vortical structures in the interstices of spherical packings.

1. Introduction

Packed beds are an essential part of many industrial processes such as waste incineration, drying, roasting, pyrolysis, calcination, and sintering. The gas flow through the interstices of a packed bed has important effects on the heat and mass transfer in it. A detailed understanding of the flow is therefore essential for the optimization of processes based on packed beds. Particle Image Velocimetry (PIV) is a non-intrusive optical measurement technique that provides velocity fields when optical access is possible. In a packed bed, however, bulk particles are typically opaque, blocking the line of sight. Optical access can be restored by using transparent particles. This, however, results in optical distortions that need to be corrected before a velocity field can be reconstructed with standard techniques. The most common approach for the correction is refractive index matching, e.g. (Harshani et al., 2017; Larsson et al., 2018; Meinicke et al., 2017; Nguyen et al., 2018; Patil & Liburdy, 2015; Wu & Mirbod, 2018). Due to the high refractive indices of commonly used transparent materials, such as PMMA or borosilicate glass, refractive index matching is only available for liquids. An alternative technique is presented by Martins et al. where distorted particle fields are corrected using a ray tracing simulation of the light propagation in the transparent packed bed.

In the present work, the approach of Martins et al. is extended and applied to a well-defined packed bed consisting of 40mm spheres in body centred cubic (bcc) arrangement. This includes an optimization of the optical simulation that scales to higher resolutions. The reconstruction of flow velocity fields in the surface layers behind transparent glass spheres and their surroundings are demonstrated for particle Reynolds numbers Re_P between 200 to 500 (based on the particle diameter d_P and the theoretical porosity of a bcc-packing ($\varphi=0.32$)).
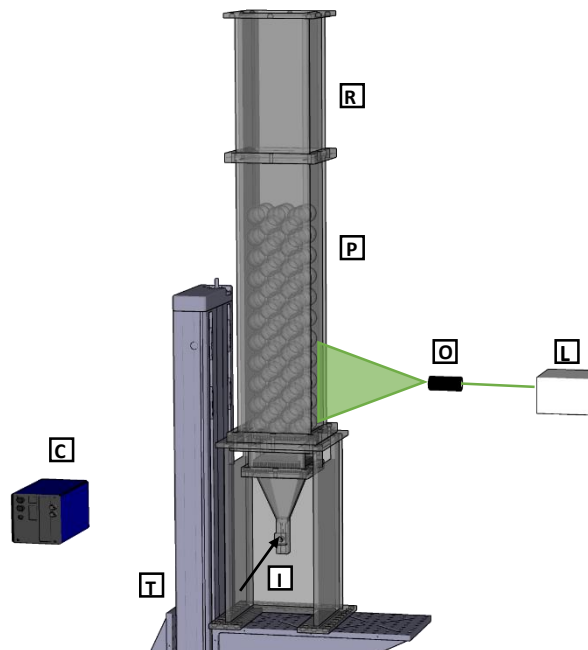
2. Experimental Setup

Fig. 1 Experimental setup consisting of a bulk reactor (R), the bcc-packing (P), the air inlet (I), the PIV-laser (L), the camera (C), the light sheet optics (O) and a 3D-traversing system (T).

The experimental setup for the PIV measurement in a transparent packed bed is shown in Fig.1. A specially designed reactor (R) is used to hold up to 21 layers of 40mm spheres in a bcc-packing (P) with 3x3 spheres in the base and all following odd layers. For optical access in the measurement zones the reactor consists of acrylic glass. High quality $d_P=40mm$ N-BK7 ball lenses from Knight Optical (UK) Ltd. are used as bulk particles in the optical paths and the rest of the packing is filled with less expensive polyethylene precision balls. Layers where no measurements are carried out were connected by the use of a melting adhesive to disable the movement of single spheres and ensure reproducibility of the packing. Pressurised air controlled by a Bronkhorst Mass-Stream Controller (D-6371; 500 l/min air) is entering the reactor through the inlet (I) together with vapourized Di-Ethyl-Hexyl-Sebacat (DEHS) as liquid tracer particles which are provided by a liquid nebulizer Type AGF 10.0 from Palas GmbH. To ensure regular and symmetric gas repartition, the flow is distributed over the entire cross section by a diffuser in combination with a honeycomb and a random packing of $d=4mm$ glass spheres and homogenised by a second honeycomb and further three layers of spheres before entering the bcc-packing through a ground plate. Bearings embedded in the ground plate hold the $d_P=40mm$ spheres of the packing in place to guarantee in combination with the walls of the reactor the stabilisation of the bcc-packing. An additional hole pattern distributed over the ground plate with $d=4mm$ holes leads to a defined gas

flow entering the packing. To reduce wall effects, this pattern is omitted in the rim region. Moving the reactor by an Isel 3D-traversing system (T) allows it to reach different measurement planes. Illumination is generated by a Quantel Q-smart Twins 850 Nd:YAG PIV-laser (L) which operates with a wavelength of 532nm, 380mJ/pulse and a frequency of 10Hz.

For signal detection an Imager LX 8M camera (C) from LaVision equipped with a 35mm Nikon micro lens is used. Attention has to be paid to the placement of the camera in combination with the used lenses. For recording standard PIV particle field images, where no ray tracing should be performed, the distance from the camera to the light sheet can be chosen to see the area of interest with an aperture of 5.6. This is the case for the measurements of the inlet condition or measurements above the packing without looking through the glass spheres. On the other hand, if ray tracing based correction should be performed, the lens and the camera parameters have to be chosen so that the measurement plane, the shifted focus plan, and the ray tracing reference target outside the reactor are in focus (see Fig. 2). This is described in more detail in the following chapter. Martins et al. (2018) also mention that a slight blur in the background has to be accepted as a result of the different focus planes and the large depth of field needed to have shown planes in focus. For the shown measurements with ray tracing based reconstruction, the distance from the camera sensor to the light sheet is 530.9mm. When recording particle field images, the blurring effect seems to be more pronounced than when recording the reference images with LED illumination. To generate the necessary depth of field, the lens is operated with an aperture of 16 as a compromise between measurement signal intensity and depth of field.
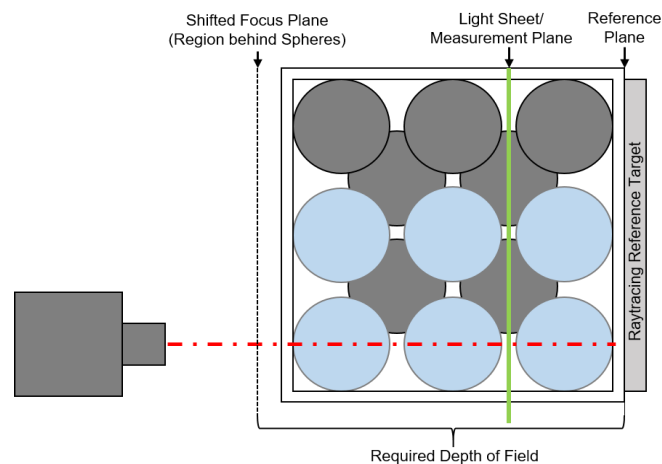
Fig. 2 Top view of the reactor's bcc sphere packing. Grey spheres represent opaque and blue spheres transparent particles. Scheme of the different focus planes for images with ray tracing based correction: the measurement plane represented by the green laser light sheet line, the shifted focus plane of the region behind the spheres on the left and the focus plane of the ray tracing reference target on the right. The red dashed line illustrates the optical axis of the camera.

Besides the particle field images, which are recorded in double frame mode with a frequency of *f=2.5Hz*, single frame images of calibration targets are recorded: a PIV calibration target (Type 10-06 from LaVision) in the measurement plane and a ray tracing calibration target with checkerboard pattern and ArUco markers, placed behind the reactor. For both calibration images the setup is illuminated by a green LED. Laser and camera are synchronised by a PTU X. The software DaVis 8 is used for control and evaluation. The ray tracing based distortion correction is based on our own in-house optical simulation described in the following section 3.

3. Ray tracing based reconstruction

The scattered light coming from the PIV tracer particles is reflected and refracted at the transparent spheres, leading to distortion in the recorded images. This has to be corrected before standard PIV software, such as DaVis, can be used for velocity vector field calculation. Following (Martins et al., 2018), an optical simulation of the light propagation is used for correction.

For this the acquired image is considered as a light source, the light field is traced back to its original configuration in the apparatus by exploiting the reversibility of light transport, and then the image that would have been obtained without the transparent spheres is computed. This is schematically depicted in Fig. 3.
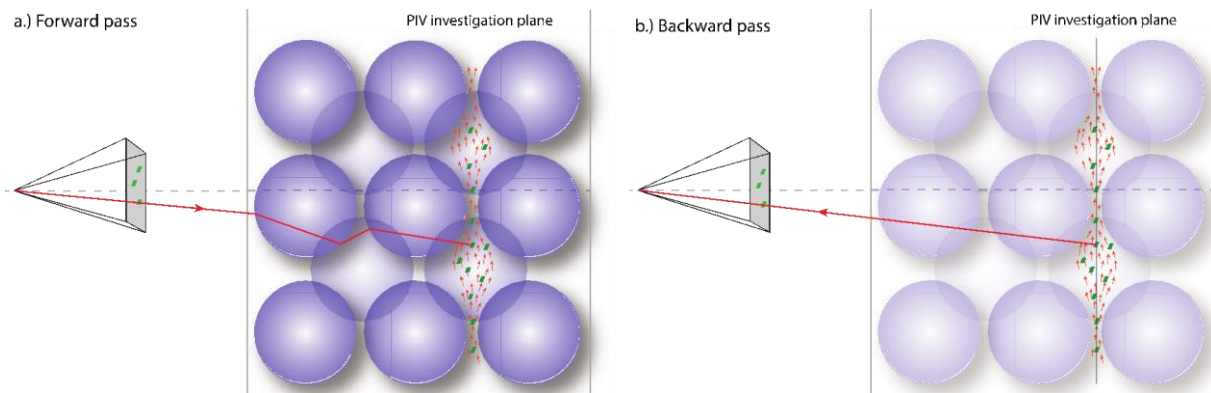

Fig. 3 Schematic depiction of the optical simulation (top view): To correct for the distortion we first perform a forward ray tracing pass that uses the captured image from the real experiment as source and reconstructs the light distribution associated with particles in the apparatus (left). In a second backward ray tracing step we compute the image that would have been obtained without the transparent spheres by removing them in the computer model (indicated through the pale shading on the right).

In our previous work (Martins et al., 2018), a mapping was precomputed that described explicitly how a pixel value in the captured image contributes to all other pixels in the undistorted one. With state-of-the-art camera resolutions, this led to very large storage requirements (≈100 GB) for the mapping. In the present work, the mapping is not computed explicitly but its effect is determined on the fly using efficient light transport simulation with no appreciable impact on performance.

The detailed reconstruction steps are as follows. First a 3D computer model of the experimental apparatus is generated; in our case this was directly available from the CAD files of the reactor. Discrepancies that arise from manufacturing tolerances or material inhomogeneities (in particular in the transparent spheres) are thereby currently ignored. To account for the complex camera system, which would be too difficult to model explicitly, intrinsic and extrinsic camera calibration is performed assuming a pinhole camera model with a lens distortion, as it is implemented in the LaVision DaVis Software as well as the OpenCV library (Bradski, 2000). Since the intrinsic parameters remain unchanged for a specific set-up, it is carried out in an offline step prior to a measurement series. For the extrinsic calibration, we use ArUco markers as available in the OpenCV library (Bradski, 2000). These are placed behind the transparent packed bed in the apparatus so that they are visible in the acquired images. Once the camera calibration is complete, the captured image is used as source and ray tracing is performed to compute the original light field distribution on the PIV investigation field (see Fig. 3 left). This is then the input for a second

ray tracing pass with a computer model of the experimental apparatus where the distortion-causing transparent spheres have been removed (Fig. 3 right). This results in a distortion-free imaging of the tracer field that can be used as input for standard PIV software. For ray tracing, we use a modified version of the open source PBRT software (Pharr & Humphreys, 2010), that we extended to obtain complete information of the light paths in the experimental apparatus and by a custom sensor that records the light field distribution on the PIV investigation field.

4. Inlet Conditions and Bed Height Independent Flow

The bulk reactor is designed to be symmetrically. Therefore, symmetric averaged flow fields are expected. Due to this, the horizontal origin (x-axis) is chosen to be the centre of the reactor while the vertical axis (y-axis) provides information about the bed height above the ground plate. The depth (z-axis) is described by the camera viewing direction with its origin at the inner side of the front acrylic wall.

By PIV measurements of the flow fields at different positions above the ground plate in the empty bulk reactor without the spherical packing material, the flow symmetry has been verified. This allows later on to reduce the amount of measurements when more complex image correction and evaluation is required. The measurement planes are the centre ($z=66.19mm$), two positions symmetrically to the centre at the positions between the later first and second ($z=43.09$) and between the later second and third sphere ($z=89.29mm$). Additionally, the analogous positions for the reactor rotated by 90° around its vertical axis are considered. Measurements were carried out in a range of $Re_P=200 … 500$ based on the particle diameter $d_P=40mm$, the theoretical porosity $\varphi=0.32$ of a bcc-packing and the cross-section of the bulk reactor $A=0.0175m^2$.

In Fig. 4 the averaged flow fields of the main vertical velocity component v_y of the inlet flow for $Re_P=200$ and the aforementioned positions are shown. The flow in each position is defined by the influence of the ground plate. Front and back positions show recirculation zones close to the wall directly above the ground plate, which can be explained by the missing gas distribution holes near the wall. Also for the centred position larger recirculation zones near the wall and additionally in the middle exist, matching the positions of the bearings that hold later on the spheres.
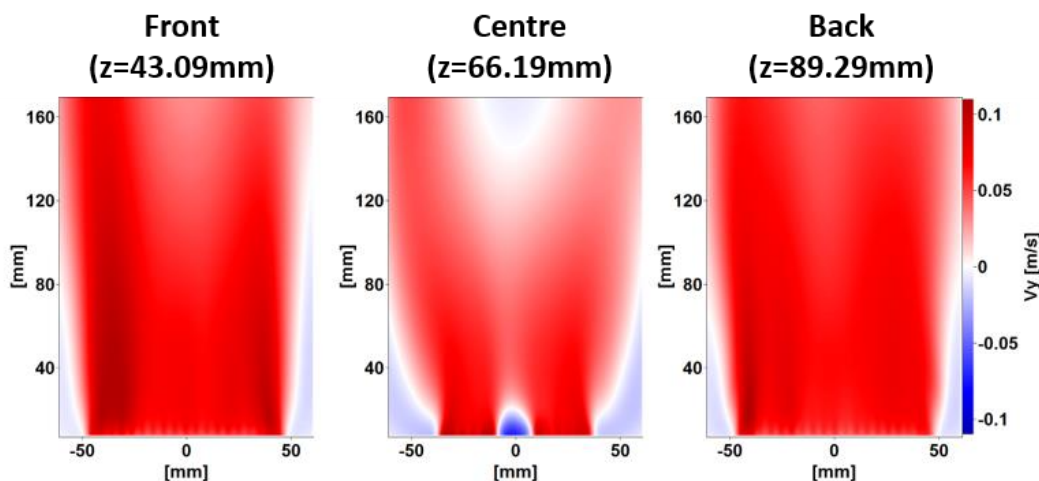

Fig. 4 Averaged vector fields of the main vertical velocity component v_y of the inlet region for $Re_P=200$ for different measurement positions (front, centre and back).
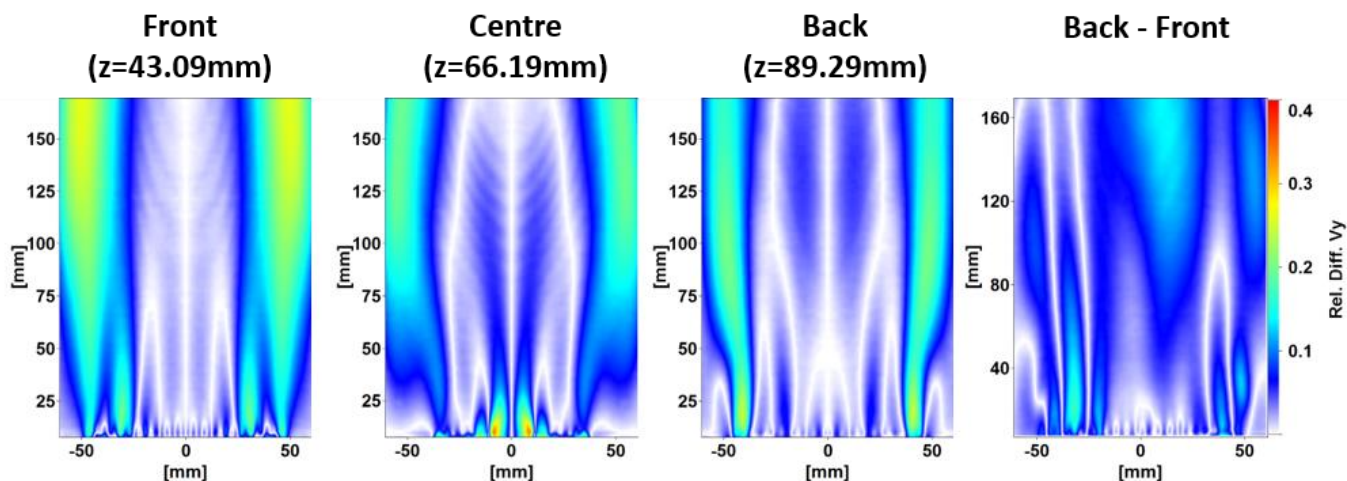
Fig. 5 Relative difference images of the main flow component v_y for different measurement positions (front, centre and back) and difference between the back and front position.

To verify the symmetry of the flow, difference images are generated, exemplarily shown for $Re_p=200$ in Fig. 5. The first three images show the symmetry of the flow for each measurement position. For this, a vertically mirrored flow field was subtracted from the original one and normalised by the maximum vertical velocity of each position. By subtracting the velocities of the back and front position, symmetry inside the box along the camera viewing direction can be found (right image in Fig. 5). Local maximum differences of around 30% appear in regions where the main flow converts into a recirculation zone close to the walls or in the centre of the reactor directly above the ground plate, where instabilities are most pronounced.

The mean relative differences for the vertical velocity component for particle Reynolds numbers in the range of 200 to 500 are shown in Fig. 6.
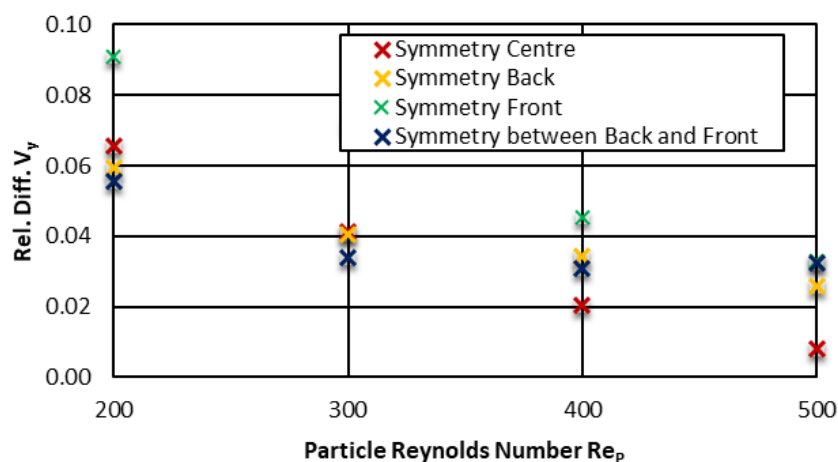

Fig. 6 Averaged relative differences of the main vertical velocity component v_y for Re_P from 200 to 500.

Relative differences do not exceed 10% in the case of $Re_P=200$, which is in the range of the measurement accuracy while higher particle Reynolds numbers come with much lower differences.

Due to the low differences, symmetrical conditions are assumed in the following so that further measurements with ray tracing based reconstruction are only carried out for z=89.29mm (between the second and third sphere). This is advantageous since measurements behind two spheres lead to a higher reconstruction zone (Martins et al., 2018).

Also for the flow field above the bed symmetrical conditions are expected. The measured averaged flow fields are shown in Fig. 7 for $Re_P=400$ above layer 17 to 21 where bed height independent flow conditions are reached.
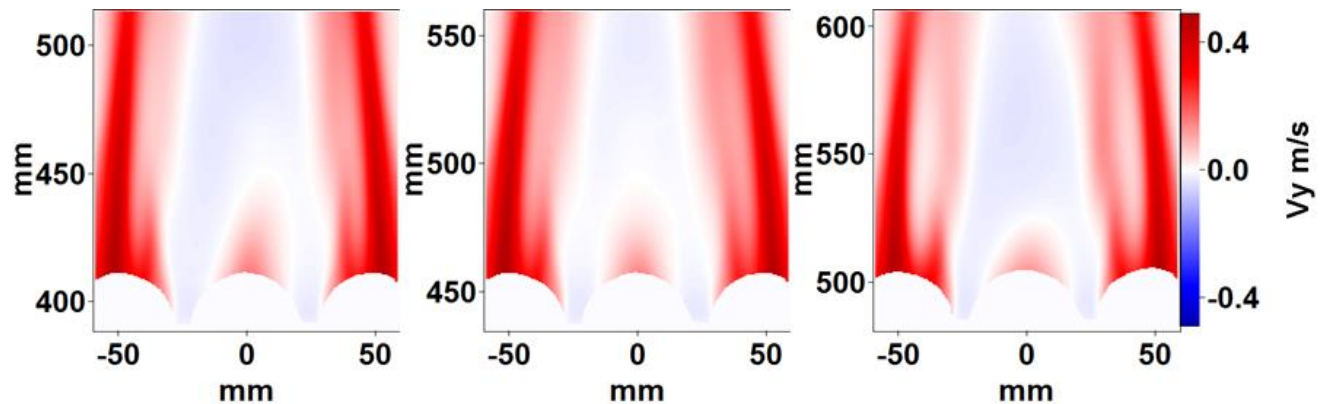

Fig. 7 Averaged velocity fields of the main vertical velocity v_y for $Re_P=400$ above layer 17 (left) to 21 (right).

The vector fields show the expected symmetrical conditions slightly varying from layer to layer. This effect is more pronounced in regions with low absolute velocities close to $v_y=0m/s$, that means in the area in and close to the recirculation zone in the centre of the reactor. The high velocities directly above the centred spheres can be explained by the pore formed by the two spheres in the underlying layer of spheres, where the flow accelerates due to the reduced cross section. The flow converts into a recirculation zone on the free surface which results from the blocked region of the underlying layer. In the rim region of the reactor the wall effect is more pronounced leading to high velocities.

The main structure of the flow fields is similar for all investigated Re_P concerning the wall effects, the appearance of recirculation zones, and regions with low velocities for $Re_P>400$. Differences only exist in the velocity shape and magnitude.

5. Method validation and results

Fig. 8 shows a comparison between an acquired raw particle field (left) and that corrected with the ray tracing simulation (right). As can be seen in the figure, the measurement plane behind the two spheres is magnified and mirrored by them. For these images, the camera was aligned to the centre of the right sphere, so that the reconstructed particle field of the centre sphere (left on the images) is shifted by the reconstruction to the right, allowing access to the rim region due to the perspective. The information in the rim region typically cannot be resolved due to strong distortion effects, as can also be seen for the right sphere.
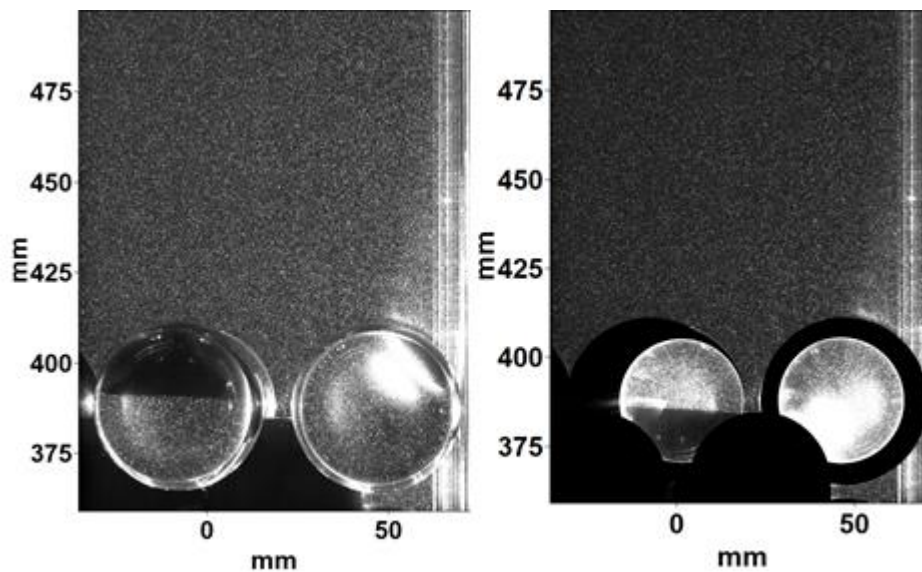
Fig. 8 Tracer particle field images before (left) and after the ray tracing based correction (right)

Already in the raw images (Fig. 8 left), regions with high intensities due to reflections or regions without any tracer particle signal can be seen. This is caused by the shadows of the underlying layer of spheres. These regions and the areas which cannot be corrected by the ray tracing based correction are masked out in the following or treated with a time filter before the PIV evaluation based on a cross-correlation method (multipass, decreasing size from 64x64 pixel to 32x32 pixel with 50% overlap) is carried out.

In Fig. 9 the vertical velocity component v_y is shown for $Re_P{=}400$ above 17 layers of spheres with and without ray tracing based correction. Already the evaluation of the particle fields without distortion correction (top left) leads to a valid vector field above the sphere packing. By applying the ray tracing based reconstruction, the particle field behind the spheres is corrected and can be evaluated. The obtained velocity field is in good agreement with the field behind the spheres and the free surface (top right). For better illustration, a magnification of the region between the two spheres is shown in the lower right image of Fig. 9. Here, the existence of a vortex in the gap in between the spheres can be seen. The flow field from the corrected region behind the spheres and the region without correction match perfectly.

The lower left image of Fig. 9 shows the relative difference of the main flow velocity v_y of the freeboard with and without distortion correction. The averaged difference is around 0.05% and local maxima do not exceed 5%. These higher values are found close to the masked regions and can be explained by the influence of the masks applied to the image before PIV evaluation. It can be assumed that no significant change is introduced by the ray tracing reconstruction of regions where no distortion exists.

Applying the method to particle fields above 17 layers of spheres and varying the particle Reynolds number leads to the averaged vertical velocity fields shown in Fig. 10. Also here a good agreement of the corrected area and the freeboard can be seen. Only in regions where strong reflections appear (e.g. lower part of right sphere), it seems to be difficult to recover all tracer particles by applying only a time filter, as is done here. Instead a mask should be applied that avoids the reflections and ensures that the correct vector field can be obtained. The flow fields themselves show similar behaviour to what was described in section 4 for the freeboard.
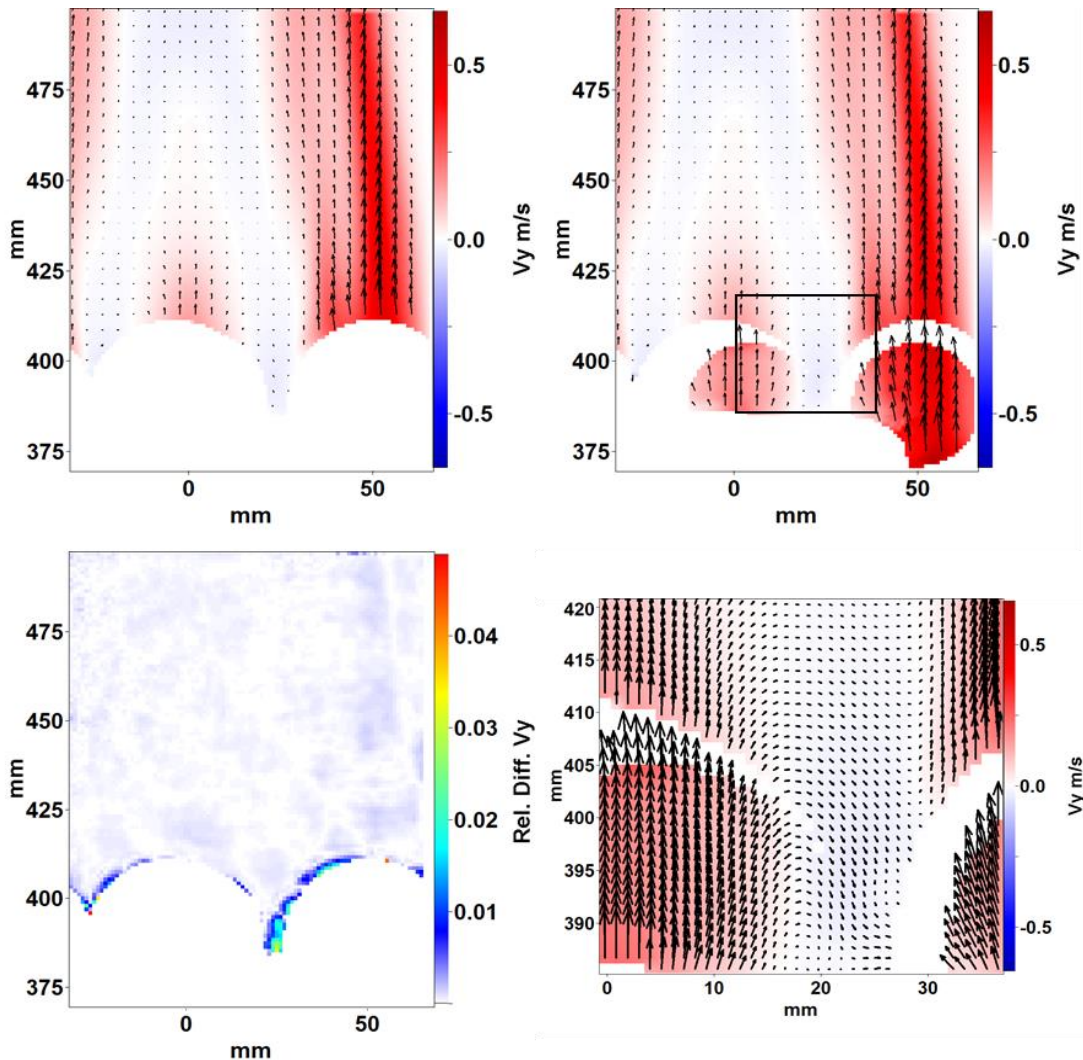
Fig. 9 Averaged vertical velocity v_y at $Re_p=400$ above 17 layers of spheres without (top left) and with (top right) distortion correction. The rectangle marks the region where the vector field is magnified (bottom right). A relative difference image (bottom left) between corrected and uncorrected images shows that the influence of the ray tracing based correction to regions where no distortion appears is neglectable.
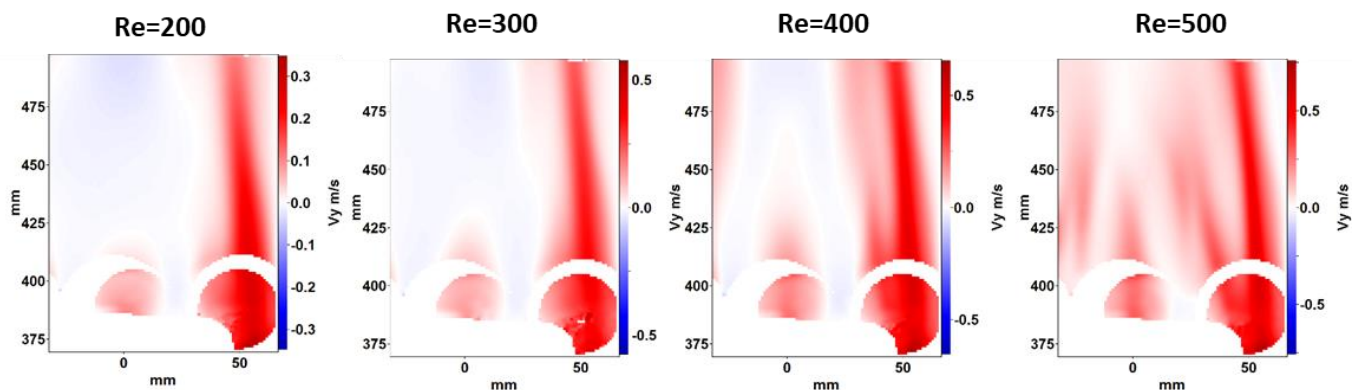

Fig. 10 Averaged vertical velocity v_y above 17 Layers of spheres for $Re_P=200$ to 500 with distortion correction.

Vertical velocity profiles of the main velocity component v_y in different positions (Pos. 1 around 0mm, Pos. 2 around 20mm, Pos. 3 around 55mm) are shown in Fig. 11. The figure demonstrates the effectiveness of the ray tracing based correction through the continuity of the velocity profiles in the surrounding free board and behind the distortion causing spheres. Pos. 1 and 3 (top and bottom left images) were chosen because of the applied masks, which can be seen clearly in the diagrams through the missing values (white). For both positions, the flow behaviour for the different particle Reynolds numbers is similar and they only differ in the velocity magnitude as described before in section 3. Further, the velocity profiles are continuous over the position of the masks. The profile for Pos. 2 *$Re_P=500$* differs significantly from the other particle Reynolds numbers. Here, the flow velocity is high enough that no recirculation zone is formed and the flow is overall more unstable.
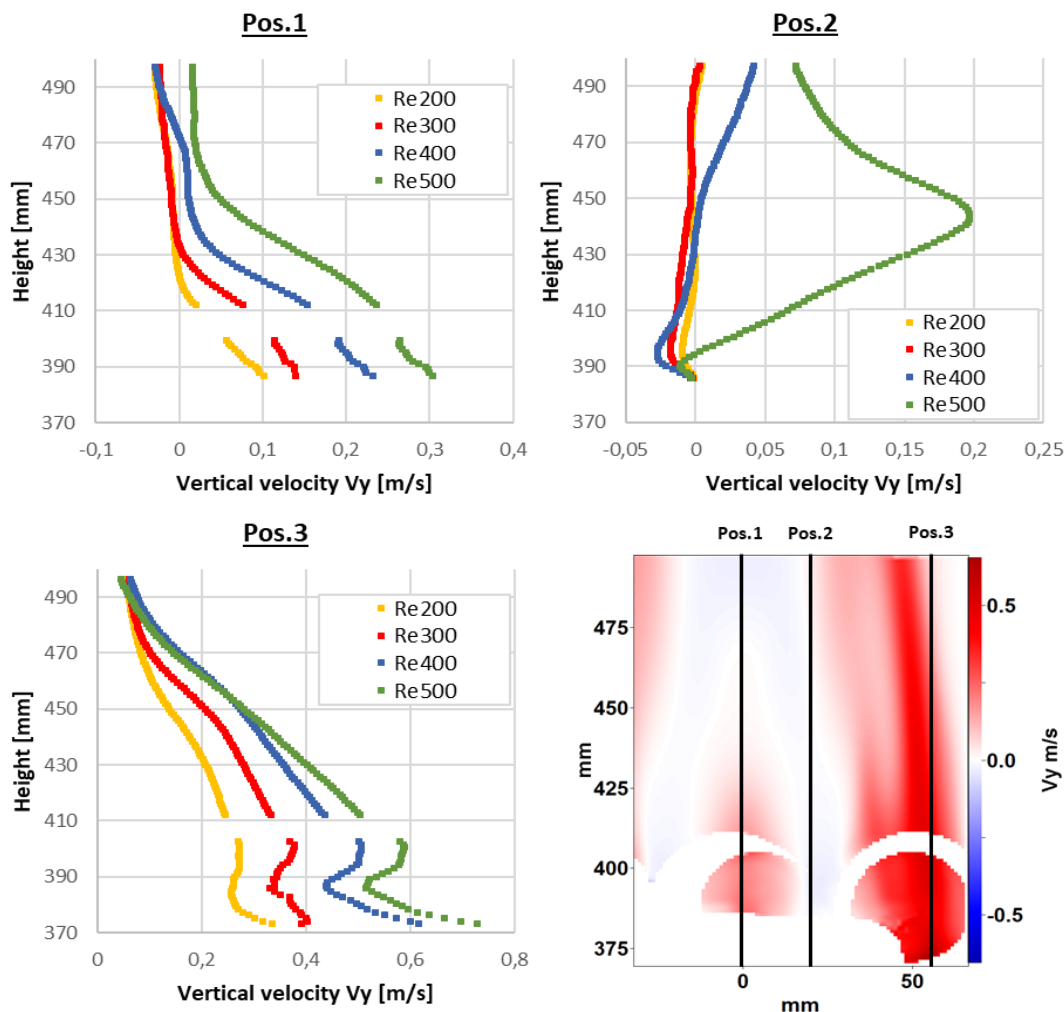
Fig. 11 Velocity profiles of the averaged vertical velocity component v_y for three different positions for *$Re_P=200...500$*.

6. Conclusion

In this study, the flow field behind the surface spheres of a packed bed is determined by PIV in combination with ray tracing based reconstruction. The presented improved reconstruction method allows for PIV in packed beds where it would otherwise be very challenging to obtain high resolution velocity field measurements. We showed that the reconstruction of the velocity

field in distorted regions delivers good results which are in agreement with the freeboard flow field. Flow field results for particle Reynolds numbers from 200 to 500 were provided for a packed bed of 17 layers where already inlet independent conditions were obtained. For future work it will be important to access also the rim regions of the spheres, where distortion is difficult to correct. One possibility could be a perspective image acquisition as obtained for the centre sphere. Here it was possible to reconstruct the rim region of this sphere. By applying different perspectives to a sphere, e.g. in successive images, the entire region behind it should be accessible.

Acknowledgements

References

Bradski, G. (2000). OpenCV. *Dr. Dobb's Journal: Software Tools for the Professional Programmer, 25*(11), 120-123.

Harshani, H. M. D., Galindo-Torres, S. A., Scheuermann, A., & Muhlhaus, H. B. (2017). Experimental study of porous media flow using hydro-gel beads and LED based PIV. *Measurement Science and Technology, 28*(1), 015902.

Larsson, I. A. S., Lundström, T. S., & Lycksam, H. (2018). Tomographic PIV of flow through ordered thin porous media. *Experiments in Fluids, 59*(6), 96.

Martins, F., Carvalho da Silva, C., Lessig, C., & Zähringer, K. (2018). Ray-Tracing Based Image Correction of Optical Distortions for PIV Measurements in Packed Beds. *Journal of Advanced Optics and Photonics, 1*(2), 71-94.

Meinicke, S., Möller, C.-O., Dietrich, B., Schlüter, M., & Wetzel, T. (2017). Experimental and numerical investigation of single-phase hydrodynamics in glass sponges by means of combined µPIV measurements and CFD simulation. *Chemical Engineering Science, 160*, 131-143.

Nguyen, T., Kappes, E., King, S., Hassan, Y., & Ugaz, V. (2018). Time-resolved PIV measurements in a low-aspect ratio facility of randomly packed spheres and flow analysis using modal decomposition. *Experiments in Fluids, 59*(8), 127.

Patil, V. A., & Liburdy, J. A. (2015). Scale estimation for turbulent flows in porous media. *Chemical Engineering Science, 123*, 231-235.

Pharr, M., & Humphreys, G. (2010). *Physically Based Rendering: From Theory to Implementation* (second ed.). San Francisco, CA, USA: Morgan Kaufmann Publishers Inc.

Wu, Z., & Mirbod, P. (2018). Experimental analysis of the flow near the boundary of random porous media. *Physics of Fluids, 30*(4), 047103.